

Generation of adaptive coordinates and their use in the Fourier Modal Method

Sabine Essig and Kurt Busch

Institut für Theoretische Festkörperphysik and DFG-Center for Functional Nanostructures (CFN), Karlsruher Institut für Technologie (KIT), Wolfgang-Gaede-Str. 1, 76131 Karlsruhe, Germany

kurt.busch@kit.edu

Abstract: We present an improvement of the standard Fourier Modal Method (FMM) for the analysis of lamellar gratings that is based on the use of *automatically generated* adaptive coordinates for arbitrarily shaped material profiles in the lateral plane of periodicity. This allows for an accurate resolution of small geometric features and/or large material contrasts within the unit. For dielectric gratings, we obtain considerable convergence accelerations. Similarly, for metallic gratings, our approach allows efficient and accurate computations of transmittance and reflectance coefficients into various Bragg orders, the spectral positions of Rayleigh anomalies, and field enhancement values within the grating structures.

© 2010 Optical Society of America

OCIS codes: (090.1970) Diffractive optics; (160.5298) Photonic crystals; (160.3918) Metamaterials; (050.1755) Computational electromagnetic methods.

References and links

1. K. Busch, G. von Freymann, S. Linden, S. F. Mingaleev, L. Tkeshelashvili, and M. Wegener, "Periodic nanostructures for photonics," *Phys. Rep.* **444**, 101–202 (2007).
2. F. J. Garcia de Abajo, "Light scattering by particle and hole arrays," *Rev. Mod. Phys.* **79**, 1267–1290 (2007).
3. M. E. Stewart, C. R. Anderton, L. B. Thompson, J. Maria, S. K. Gray, J. A. Rogers, and R. G. Nuzzo, "Nanostructured plasmonic sensors," *Chem. Rev.* **108**, 494–521 (2008).
4. M. G. Moharam and T. K. Gaylord, "Diffraction analysis of dielectric surface-relief gratings," *J. Opt. Soc. Am.* **72**, 1385–1392 (1982).
5. M. G. Moharam, E. B. Grann, D. A. Pommet, and T. K. Gaylord, "Formulation of stable and efficient implementation of the rigorous coupled-wave analysis of binary gratings," *J. Opt. Soc. Am. A* **12**, 1068–1076 (1995).
6. P. Lalanne and G. M. Morris, "Highly improved convergence of the coupled-wave method for TM polarization," *J. Opt. Soc. Am. A* **13**, 779–784 (1996).
7. G. Granet and B. Guizal, "Efficient implementation of the coupled-wave method for metallic lamellar gratings in TM polarization," *J. Opt. Soc. Am. A* **13**, 1019–1023 (1996).
8. L. Li, "Use of Fourier series in the analysis of discontinuous periodic structures," *J. Opt. Soc. Am. A* **13**, 1870–1876 (1996).
9. L. Li, "Formulation and comparison of two recursive matrix algorithms for modeling layered diffraction gratings," *J. Opt. Soc. Am. A* **13**, 1024–1034 (1996).
10. L. Li, "New formulation of the Fourier modal method for crossed surface-relief gratings," *J. Opt. Soc. Am. A* **14**, 2758–2767 (1997).
11. M. Nevière and E. Popov, *Light propagation in periodic media: Differential theory and design*, (Marcel Dekker, New York, 2003).
12. T. Schuster, J. Ruoff, N. Kerwien, Rafler, and W. Osten, "Normal vector method for convergence improvement using the RCWA for crossed gratings," *J. Opt. Soc. Am. A* **24**, 2880–2890 (2007).
13. G. Granet, "Reformulation of the lamellar grating problem through the concept of adaptive spatial resolution," *J. Opt. Soc. Am. A* **16**, 2510–2516 (1999).
14. J. Chandezon, M. T. Dupuis, G. Gornet, and D. Maystre, "Multicoated gratings: a differential formalism applicable in the entire optical region," *J. Opt. Soc. Am.* **72**, 839–846 (1982).

15. T. Vallius and M. Honkanen, "Reformulation of the Fourier modal method with adaptive spatial resolution: application to multilevel profiles," *Opt. Express* **10**, 24–34 (2002).
16. G. Granet and J.-P. Plumey, "Parametric formulation of the Fourier modal method for crossed surface-relief gratings," *J. Opt. A* **4**, S145–S149 (2002).
17. T. Weiss, G. Granet, N. A. Gippius, S. G. Tikhodeev, and H. Giessen, "Matched coordinates and adaptive spatial resolution in the Fourier modal method," *Opt. Express* **17**, 8051–8061 (2009).
18. U. Leonhardt and T. G. Philbin, "General relativity in electrical engineering," *N. J. Phys.* **8**, 247 (2006).
19. A. Greenleaf, Y. Kurylev, M. Lassas, and G. Uhlmann, "Cloaking devices, electromagnetic wormholes, and transformation optics," *SIAM Review* **51**, 3–33 (2009).
20. G. J. Pearce, T. D. Hedley, and D. M. Bird, "Adaptive curvilinear coordinates in a plane-wave solution of Maxwell's equations in photonic crystals," *Phys. Rev. B* **71**, 195108 (2005).
21. F. Gygi, "Electronic-structure calculations in adaptive coordinates," *Phys. Rev. B* **48**, 11692–11700 (1993).
22. P. Götz, T. Schuster, K. Frenner, S. Rafler, and W. Osten, "Normal vector method for the RCWA with automated vector field generation," *Opt. Express* **16**, 17295–17301 (2008).
23. L. Li, "Fourier modal method for crossed anisotropic gratings with arbitrary permittivity and permeability tensors," *J. Opt. A* **5**, 345–355 (2003).
24. L. Li, "Note on the S-matrix propagation algorithm," *J. Opt. Soc. Am. A* **20**, 655–660 (2003).
25. G. Granet and B. Guizal, "Analysis of strip gratings using a parametric modal method by Fourier expansions," *Opt. Commun.* **255**, 1–11 (2005).
26. <http://www.gnu.org>.
27. A. Vial, A.-S. Grimault, D. Macías, D. Barchiesi, and M. Lamy de la Chapelle, "Improved analytical fit of gold dispersion: Application to the modeling of extinction spectra with a finite-difference time-domain method," *Phys. Rev. B* **71**, 085416 (2005).
28. B. Bai and L. Li, "Group-theoretic approach to enhancing the Fourier modal method for crossed gratings with C_4 symmetry," *J. Opt. A* **7**, 783–789 (2005).
29. J. S. Shumaker-Parry, H. Rochholz, and M. Kreiter, "Fabrication of Crescent-Shaped Optical Antennas," *Adv. Mater.* **17**, 2131–2134 (2005).
30. H. Rochholz, N. Bocchio, and M. Kreiter, "Tuning resonances on crescent-shaped noble-metal nanoparticles," *N. J. Phys.* **9**, 53 (2007).
31. Y. Choi, S. Hong, and L. P. Lee, "Shadow Overlap Ion-beam Lithography for Nanoarchitectures," *Nano Lett.* **9**, 3726–3731 (2009).

1. Introduction

Periodic photonic nanostructures, such as photonic crystals and metamaterials [1] as well as periodically structured surfaces [2, 3], may exhibit interesting optical responses that can be exploited for numerous applications. Both, a sufficient understanding of the underlying physics as well as the engineering of certain desired optical properties require efficient computational tools. In this context, the Fourier Modal Method (FMM), also known as the Rigorous Coupled-Wave Analysis (RCWA), has proven to be an adequate and commonly used method for the numerical analysis of the resulting grating or grating-like structures [4–8]. Thus, FMM has been used to characterize a good many of structured optical materials as well as to develop numerous optimized designs.

The FMM treats three-dimensional systems with a strict periodicity in the lateral plane by decomposing the structure in the third direction (the propagation direction) into a sequence of two-dimensional subsystems – the so-called slices. Within each slice, the material parameters in the propagation direction are assumed to be constant, thus admitting propagating or evanescent plane wave solutions. Consequently, in each slice Maxwell's equations are solved via an eigenvalue equation for the (generally complex-valued) wave vectors and associated eigenmodes in propagation direction. The lateral periodicity is accounted for via the Bloch-Floquet theorem for the real-valued lateral wave vector. Finally, in each slice the field is expanded into the corresponding eigenmodes and the slices are recombined to represent the complete system by applying appropriate boundary conditions across the interfaces between adjacent slices via a scattering matrix formalism [9].

In view of the nature of the available fabrication techniques, many systems can be represented by spatially discontinuous permittivity functions. Since FMM solves Maxwell's equations in

Fourier space, such discontinuities can quickly lead to unsatisfactory convergence characteristics. Nevertheless, by carefully performing the transformation from real-space permittivity profiles into Fourier series representations, the convergence of one-dimensional lamellar gratings could be dramatically improved [6, 7]. In Ref. [8], Li has formulated two rules, the so-called Fourier factorization rules, that provide a rigorous mathematical foundation for the correct Fourier expansion of such permittivity profiles. As a result, improved convergence characteristics could also be realized for crossed gratings [10]. However, for complex material profiles within the unit cell the material boundaries are generally not aligned to the coordinate axes. In this case, the Fourier factorization rules cannot be applied to the actual contour of the material boundaries but to a stair-cased, i.e., zigzag-shaped approximate contour. This leads to particular serious convergence problems for non-grid aligned metallic structures (see section 4.2 below).

In response to this, different approaches have been developed to further improve convergence. For instance, in order to avoid Li's zig-zag method, the use of normal vectors similar to the differential method has been suggested [11, 12]. Then, the Fourier factorization rules can be applied more effectively to the actual structural contours. In a separate development, Granet has introduced adaptive coordinates that aim at improving the sampling of material boundaries [13]. In contrast to the Chandezon method [14] where a coordinate transformation along the propagation direction maps the grating surface profile onto a (flat) plane, the Granet method introduces a coordinate transformation in the lateral plane that increases the spatial resolution at the material boundaries. This procedure considerably speeds up the convergence of the Fourier-transform representation of discontinuous permittivity profiles. In case of several slices with different profiles in different layers, the transformations may also differ from slice to slice [15]. The idea of adaptive spatial resolution (ASR) has also been extended to crossed gratings [16, 17]. Ideally, the coordinate lines of the emerging curvilinear coordinates should be aligned along the structural contours. These curvilinear meshes are incorporated into Maxwell's equations via the same formalism that is commonly used in transformation optics [18, 19]. Conversely, one may regard the use of ASR as another application of transformation optics (see section 2 below).

Since the formulation of ASR within FMM is straightforward, the primary problem is to find a coordinate transformation that is adapted to a given structure (e.g., as shown in Figs. 3, 5, and 8). As stated above, this coordinate transformation shall increase the point density at material interfaces and shall guide the coordinate lines along the interfaces such that the structure is locally aligned relative to the new local coordinate system. Obviously, it is highly desirable that this coordinate transformation can be *automatically generated* and can thus be applied to arbitrary material profiles. This has not yet been fully accomplished in the early pioneering works [15–17]. More precisely, Refs. [15, 16] have been restricted to factorizable coordinate transformations, i.e., to cases where the two-dimensional coordinate transform can be represented as the product of two one-dimensional transformations. For the latter, analytical expressions can be found [13]. More general is the approach reported in Ref. [17]. Here, the coordinate transformation is explicitly constructed by manually subdividing the unit cell into patches that (i) can isomorphically be mapped onto rectangles and (ii) have their corners either on the outer boundary of the unit cell or on a material interface. While this significantly improves the range of applicability of ASR within FMM, it has not yet been demonstrated how this subdivision can be automatized and whether such a subdivision always exists for more complex material distributions and/or structural contours within the unit cell.

In the case of photonic [20] and electronic [21] bandstructure calculations it has already been shown how adaptive curvilinear coordinates can be generated automatically. Additionally, in Ref. [22] it is shown how a vector field which is normal to the material interfaces can be generated in order to avoid Li's zig-zag method.

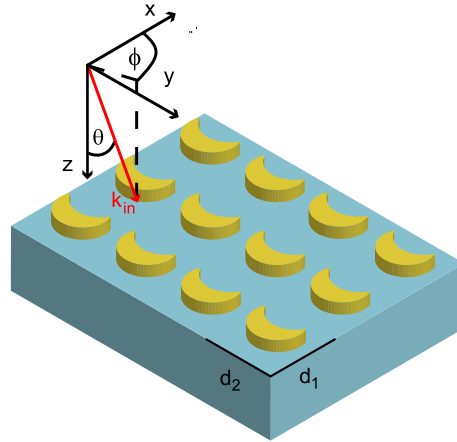


Fig. 1. Illustration of a crossed-grating in the Cartesian coordinate system $O\bar{x}^1\bar{x}^2\bar{x}^3 \equiv Oxyz$. The system is periodic in the \bar{x}^1 - and \bar{x}^2 -directions with periodicities d_1 and d_2 , respectively. The grating is illuminated by a plane wave with wave vector \mathbf{k}_{in} whose direction defines the polar angle ϕ and the azimuthal angle θ .

This is the starting point of our work. In particular, similar to [20, 21], we set up a fictitious energy functional that allows us to derive adaptive curvilinear coordinates through a standard minimization procedure. This fictitious energy functional is characterized by certain terms that implement the above-mentioned desired properties whose relative weights can be flexibly adjusted. In addition, we augment the energy functional of Refs. [20, 21] by a term that is inspired by the results of Ref. [22] in that it helps to locally align one of the coordinate lines relative to material interfaces. Consequently, we will first review the FMM in general coordinate systems in section 2. Then, in section 3 we provide the details of our approach for the generation of coordinate transformations by minimizing a fictitious energy functional. This automated coordinate generation will subsequently be applied to different systems with dielectric and metallic constituent materials. More precisely, simple test structures are investigated in section 4. For these systems, we provide convergence analyses and compare our results with those that are obtained via analytically available adaptive coordinates [16, 17]. In section 5, a more complex structure is analyzed. Finally, we conclude our findings in section 6.

2. Fourier Modal Method in general coordinates

We consider systems within a Cartesian coordinate system $O\bar{x}^1\bar{x}^2\bar{x}^3$ that are periodic in the (lateral) $\bar{x}^1\bar{x}^2$ -plane and finite in the \bar{x}^3 -direction, the propagation direction (see Fig. 1). A plane wave with wave vector \mathbf{k}_{in} is incident on this structure and the direction of the wave vector defines the polar angle and azimuthal angles, ϕ and θ . For concreteness and since this is a rather often occurring setup [2, 3], we examine in this work only systems that consist of three regions each of which is homogeneous in propagation direction: (i) a semi-infinite superstrate region in which the incoming radiation is specified and the radiation that is reflected into certain Bragg orders has to be determined, (ii) a lateral, periodically structured lamellar grating of height h , and (iii) a semi-infinite substrate region in which the radiation that is transmitted into certain Bragg orders has to be determined.

For simplicity, we assume that the grating region is composed of rectangular unit cells with side lengths d_1 and d_2 that contain a distribution of isotropic and nonmagnetic dielectric materials whose profile is described by $\bar{\epsilon}(\bar{x}^1, \bar{x}^2)$. The corresponding constituent materials are

thus described via frequency-dependent complex dielectric constants and this includes many dispersive materials, notably metals. However, we would like to note that the subsequent developments can easily be extended to optically anisotropic materials such as liquid crystals and non-rectangular systems such as hexagonal arrays.

In the following, we choose to work with the covariant formulation of Maxwell's equations which allows for a straightforward incorporation of curvilinear coordinates within the FMM. Thus, we follow the notation in [23] and define a curvilinear coordinate system $Ox^1x^2x^3$ that is connected to the original Cartesian system ($O\bar{x}^1\bar{x}^2\bar{x}^3 \equiv Oxyz$) via

$$\bar{x}^1 = \bar{x}^1(x^1, x^2), \quad (1)$$

$$\bar{x}^2 = \bar{x}^2(x^1, x^2), \quad (2)$$

$$\bar{x}^3 = x^3. \quad (3)$$

Since our goal is to develop adaptive spatial resolution (ASR) within the lateral grating plane, we have restricted the coordinate transformation (1)-(3) accordingly and further require that the transformation retains the periodicity in the lateral plane with periodicities d_1 and d_2 in \bar{x}^1 - and \bar{x}^2 -direction, respectively. The contravariant metric tensor associated with these curvilinear coordinates is defined as

$$g^{kl} = \sum_{n=1}^3 \frac{\partial x^k}{\partial \bar{x}^n} \frac{\partial x^l}{\partial \bar{x}^n}. \quad (4)$$

As a consequence, we obtain the covariant form of Maxwell's curl equations for our material distribution as

$$\xi^{klm} \partial_l E_m = ik_0 \sqrt{g} g^{kl} H_l, \quad (5)$$

$$\xi^{klm} \partial_l H_m = -ik_0 \bar{\epsilon} \sqrt{g} g^{kl} E_l. \quad (6)$$

Here, E_m and H_m denote, respectively, the covariant electric and magnetic field components and we have introduced the vacuum wave number $k_0 = \omega/c$. Furthermore, g represents the reciprocal of the determinant of the metric tensor (4), ξ is the (totally antisymmetric) Levi-Civita tensor, and ∂_l is an abbreviation for $\partial/\partial x_l$.

In the above equations, (5) and (6), we can identify effective anisotropic permittivity and permeability tensors

$$\epsilon^{kl} = \bar{\epsilon} \sqrt{g} g^{kl}, \quad (7)$$

$$\mu^{kl} = \sqrt{g} g^{kl}, \quad (8)$$

that have been induced by the curvilinear coordinates. This permits us to utilize Maxwell's equations for anisotropic materials with principal axis along the \bar{x}^3 -direction for which the application of FMM (including the use of Fourier factorization rules) has been described by Li [23].

Since we apply the coordinate transformation throughout the entire system, we can in all three regions expand each of the electric or magnetic field components in the x^1x^2 -plane into a Floquet-Fourier series

$$F_\sigma(x^1, x^2, x^3) = \sum_{m,n} f_{\sigma mn}(x^3) \exp(i\alpha_m x^1 + i\beta_n x^2). \quad (9)$$

Here, F_σ ($F = E, H$ and $\sigma = 1, 2, 3$) stands for any field component with corresponding Floquet-Fourier coefficients $f_{\sigma mn}$ and we have introduced the abbreviation $\alpha_m = k_{in} \sin \theta \cos \phi + m2\pi/d_1$ and $\beta_n = k_{in} \sin \theta \sin \phi + n2\pi/d_2$. In an actual computation the sum over reciprocal

lattice vectors in (9) has to be truncated $m, n = 0, \pm 1, \pm 2, \dots$ so that in total N Floquet-Fourier coefficients have to be determined by solving Maxwell's equations in Fourier space. In general, we select those N reciprocal lattice vectors $(m2\pi/d_1, n2\pi/d_2)$ that lie closest to the origin in reciprocal space. This allows for the most flexible representation of an arbitrary material distribution inside the unit cell. Different choices would be possible for special geometries in the unit cell. However, our (rather extensive) experience indicates that this leads to only marginal improvements in the convergence rates.

When transforming the permittivity and permeability tensor into Fourier space, special care has to be exerted so as to respect the correct Fourier factorization rules. As a matter of fact, several choices are possible and we apply the symmetrized form defined in section 5 of Ref. [23]. Explicitly, this reads

$$\hat{\epsilon} = (L_1 L_2(\epsilon) + L_2 L_1(\epsilon))/2. \quad (10)$$

Using this formula (see Ref. [23]), we can compute the Toeplitz matrices for ϵ^{kl} and μ^{kl} for the general case of general curvilinear coordinate transformations. Although we consider only isotropic materials, a general coordinate transformation will, in the transformed space, induce effective anisotropic material properties (transformation optics).

Owing to the homogeneity along the propagation direction in each region, we employ a plane wave Ansatz for x^3 -dependence

$$f_{\sigma mn}(x^3) = f_{\sigma mn} \exp(ik_3 x^3). \quad (11)$$

As a result, we are able to set up an eigenvalue problem for the propagation constant q in each region. The resulting eigenvectors are the eigenmodes in the respective region and are used as an expansion basis for the field components. The expansions in the different regions are connected in curvilinear space by a scattering matrix formalism [24] that essentially ensures the continuity of the tangential fields when moving from one region to the next. As a result, we obtain a scattering matrix for the complete system. What remains is a back-transformation to the original Cartesian coordinate system in order to determine reflectance and transmittance coefficients into the appropriate Bragg orders. In the Cartesian system, the incoming and outgoing regions can be solved by a simple Rayleigh expansion as described in Ref. [10]. In order to determine properly the reflectance and transmittance in degenerate diffraction orders, we replace the numerically calculated propagating eigenmodes by the exact Rayleigh solution in the Cartesian system which are then transformed into curvilinear space [25].

3. Generation of adaptive coordinates

As discussed in section 1, the perhaps most important point in the FMM with ASR is to find a suitable coordinate transformation which significantly increases the convergence. Good results are expected for coordinate transformations that increase the point density at the material interfaces and lead to coordinate lines that are well aligned so as to faithfully represent the structural details by way of the Fourier factorisation rules. Significant progress in this direction has been achieved [15, 17], however an automated generation of such coordinates has yet to be demonstrated.

In order to automatically generate appropriate coordinate transformations we follow Ref. [20] where a method to generate coordinate transformations for two-dimensional photonic bandstructure calculations has been presented and adopt this approach to our situation.

The fact that any suitable coordinate transformation has to respect the periodicity within the lateral plane suggests a representation of the transformation via a Fourier series

$$\bar{x}^1(x^1, x^2) = x^1 + \sum_{m,n} x_{mn}^1 \exp(im2\pi/d_1 x^1 + in2\pi/d_2 x^2), \quad (12)$$

$$\bar{x}^2(x^1, x^2) = x^2 + \sum_{m,n} x_{mn}^2 \exp(im2\pi/d_1 x^1 + in2\pi/d_2 x^2). \quad (13)$$

For actual computations, the summation over the reciprocal lattice vectors has to be truncated to a total number of M plane waves, giving a total number of $2M$ expansion coefficients, i.e., M coefficients x_{mn}^1 and M coefficients x_{mn}^2 where $m, n = 0, \pm 1, \pm 2, \dots$. We aim at the most flexible, i.e., the most symmetric representation of the transformation since this can be adapted best to general material distributions within the unit cell. Therefore, we construct this plane-wave representation by selecting the M reciprocal lattice vectors $(m2\pi/d_1 x^1, n2\pi/d_2 x^2)$ to be those that lie within a circle around the origin in reciprocal space. In general, the coefficients x_{mn}^1 and x_{mn}^2 are complex numbers but we require purely real coordinate transformations. As a result, we have to determine $2M$ free parameters.

The natural procedure for determining the expansion coefficients is to setup a fictitious energy functional that, upon minimization with respect to these coefficients, implements certain desirable features of the transformation [20, 21]. We employ a specific form of the fictitious energy functional

$$\mathcal{E} = \int dx^1 dx^2 (\mathcal{E}_c(x^1, x^2) + \mathcal{E}_s(x^1, x^2) + \mathcal{E}_g(x^1, x^2) + \mathcal{E}_t(x^1, x^2)), \quad (14)$$

which is determined by integrating several contributions over the unit cell of the system. Here, \mathcal{E}_c and \mathcal{E}_s represent, respectively, compression and shear energy [21]. These two energy terms depend on the covariant metric tensor via principle invariants such as the determinant (det) and trace (tr). They exhibit a restoring character and try to pull back the coordinates to their original form within the Cartesian frame.

Explicitly, compression and shear energy read as

$$\mathcal{E}_c(x^1, x^2) = \eta_c \det(g^{mn}), \quad (15)$$

$$\mathcal{E}_s(x^1, x^2) = \eta_s \text{tr}(g^{mn}). \quad (16)$$

In these expressions, the adjustable constants η_c and η_s control the relative strength of these two energy terms within the functional. Similar to the work of Pearce et al. [20], we find that our results do not depend on using either one of the terms or both simultaneously. Thus, we do not use the shear energy and set $\eta_s = 0$.

The second set of energy terms, \mathcal{E}_g and \mathcal{E}_t , are responsible for adapting the coordinates to the geometry of the material profile contained in the unit cell as described by the permittivity distribution $\mathcal{E}(x^1, x^2)$. For the subsequent discussion, we assume that we are dealing with a binary grating, i.e., that we have two constituent materials within the unit cell, a host material matrix in which certain patches of a guest material are embedded. Since our curvilinear coordinates should faithfully represent the structural details without reference to the actual permittivity values of the host and guest material, we characterize the structural information via the function $S(x^1, x^2)$. This function takes the values 0 or 1 for points (x^1, x^2) that, respectively, lie in the host or guest material regions. Since the gradient of $S(x^1, x^2)$ is ill-defined at step-like material interfaces, we apply a Gaussian smoothing to the structure function $S(x^1, x^2)$. This smoothing is performed in Fourier space by multiplying the Fourier coefficients of the permittivity distribution with a Gaussian (filter) function. As a result, the smoothed structure function $S_{\text{sm}}(\bar{x}^1, \bar{x}^2)$ in real space is

$$S_{\text{sm}}(\bar{x}^1, \bar{x}^2) = \sum_{p,q} S_{\text{sm},pq} e^{ip2\pi/d_1 \bar{x}^1 + iq2\pi/d_2 \bar{x}^2}, \quad (17)$$

where we have introduced the smoothing width w_s and the smoothed Fourier coefficients

$$S_{\text{sm},pq} = \exp(-((2\pi/d_1 p)^2 + (2\pi/d_2 q)^2)/2w_s^2) S_{pq} \quad (18)$$

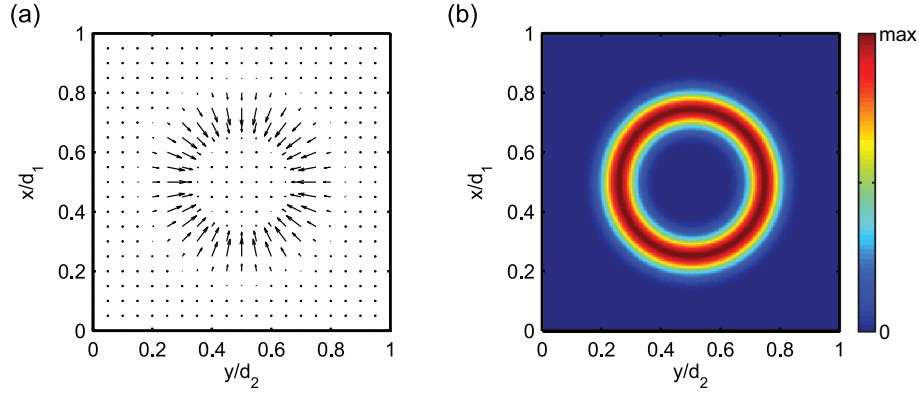


Fig. 2. Illustration of the gradient of a smoothed structure function ($w_s = 25$) for a circular-shaped patch (radius r) of guest material in the center of a quadratic unit cell ($r/d_1 = r/d_2 = 0.25$): Panel (a) displays the gradient field and panel (b) shows the relative magnitude of the gradient vectors with better spatial resolution.

that are obtained from the Fourier coefficients S_{pq} of the structure function $S(x^1, x^2)$. As a result, the gradient of the smoothed structure function yields a vector field whose vectors are locally normal to the material interfaces in a vicinity of the interface and accept their largest magnitude directly at the interface. In Fig. 2, we display this vector field for a single circular patch of a guest material that lies at the center of a quadratic unit cell.

After this preprocessing step (which would be absent for a continuously varying material distribution), we can now define an energy term \mathcal{E}_g that tends to distort coordinate lines in such a way that their density is increased in regions with large gradients of the structure function. This term has been discussed in Ref. [20] and reads

$$\mathcal{E}_g(x^1, x^2) = -|\vec{\nabla}\varepsilon_s [\bar{x}^1(x^1, x^2), \bar{x}^2(x^1, x^2)]|. \quad (19)$$

We would like to emphasize that this contribution to the fictitious energy functional does not carry a weighting factor. As a result, the weighting factors for the compression and shear contributions, η_c and η_s , as introduced above (see (15) and (16)) as well as the weighting factor η_t of the tangential contribution to be introduced below (see (20)) weight these contributions relative to the gradient contribution (19).

Furthermore and as discussed above, we also want to exploit the fact that the gradient vectors in the vicinity of material interfaces are (locally) oriented normal to material interfaces. These normal vectors have been utilized in Ref. [22] in order to improve the application of the appropriate Fourier factorization rules for field components that are tangential resp. normal to the material interfaces. In our formulation, we can take this into account via an additional contribution \mathcal{E}_t that lowers the fictitious energy (see Eq. 14) when one of the coordinate lines of the transformation (locally) runs parallel to the material interfaces. Explicitly, the tangent vectors along the coordinate lines are given by the covariant basis vectors $\mathbf{b}_1 = (\frac{\partial \bar{x}^1}{\partial x^1}, \frac{\partial \bar{x}^2}{\partial x^1})$ and $\mathbf{b}_2 = (\frac{\partial \bar{x}^1}{\partial x^2}, \frac{\partial \bar{x}^2}{\partial x^2})$, so that the scalar product between these covariant basis vectors and the gradient vector of the structure function is a direct measure of (local) parallelism of the coordinate lines relative to the material interface. Consequently, we have augmented the fictitious energy functional of Ref. [20] by

$$\mathcal{E}_t(x^1, x^2) = \eta_t \left(|\vec{\nabla}\varepsilon_s \cdot \mathbf{b}_1|^2 + |\vec{\nabla}\varepsilon_s \cdot \mathbf{b}_2|^2 \right). \quad (20)$$

To perform the minimization of this fictitious energy functional (see Eq. 14) we employ a conjugate gradient algorithm (Fletcher-Reeves), which is implemented in the gnu scientific library (gsl) [26]. The integral in the energy functional is solved by summing over a sufficiently fine discretized equidistant grid in (\bar{x}^1, \bar{x}^2) -space. Specifically, we choose the number of grid points within the unit cell such that (i) sufficient oversampling relative to the Fourier representation of the coordinate transformation is achieved and (ii) that the structural features are adequately resolved. For the results shown in this paper, we typically use a grid of 200×200 points and have checked that a finer discretization in transformed space does not change the numerical results. In order to reduce the computational complexity, we enforce the symmetry of the system onto the coordinate transformation Eq. 12 and Eq. 13 whenever possible.

4. Performance characteristics

To demonstrate the improved performance of the FMM with the automatically generated ASR, we analyze certain test systems for which reference solutions can be constructed via the ASR methods described in Refs. [15, 17]. All test systems consist of a glass substrate with permittivity $\epsilon = 2.25$ and an air superstrate ($\epsilon = 1$) that both occupy a half space. On the substrate, we deposit a single layer of periodically placed cylinders with height h and a certain cross-section which we call the motif. These patches are arranged into a square lattice such that the quadratic unit cell exhibits side lengths $d_1 = d_2 = 1000$ nm (see Fig. 1 (a)). The description of these patches of guest material is completed by specifying the material's dielectric constant ϵ . Further, we assume that host material is air so that we describe a typical monolayer of metamaterials [1] and other periodically structured surfaces [2, 3]. In our subsequent computations, we restrict ourselves to the case where these systems are normally illuminated from the air side by an incident plane wave with frequency ω and polarization \hat{e} . Oblique illumination is equally possible but the corresponding results do not provide any further insight to the workings of ASR within FMM.

Loosely speaking, there are two limiting cases of motifs which have been analyzed with the earlier ASR approaches: For completely grid-aligned motifs analytical coordinate transformations that consist of products of two one-dimensional transformations can be utilized [16, 17]. As a representative case for this class, we chose a simple square-shaped motif (corresponding to a square-disk-shaped patch of guest material with square cross-section) that is centered within the unit cell. The second, in some sense complementary case, is that of a perfectly round motif and we use a circle that is centered within the unit cell as a representative case (corresponding to a circular-disk-shaped patch of guest material). For this case, too, analytical coordinate transforms are available [17]. Furthermore, these two limiting cases also allow to test the characteristics of standard FMM: In the grid aligned case, full use of the Fourier factorization rules can be made whereas in the round case, the Fourier factorization rules will be of limited use since the Cartesian coordinate lines are, in general, not normal to the material interface and an effective stair-cased representation of the circular motif is realized (see discussion in section 1). Finally, we will carry out these test calculations for dielectric ($\epsilon = 12$) and metallic objects. In the latter case, we use a Drude model with parameters that reasonably well describe gold within the relevant frequency range (plasma frequency $\omega_p = 1.3544 \times 10^{16}$ 1/s and collision frequency $\omega_{col} = 1.1536 \times 10^{14}$ 1/s; see Ref. [27] for details).

4.1. Square disk

As a first test system, we consider an array of square disks (height $h = 50$ nm, square motif with side length $w = 500$ nm; see Fig. 3) so that the disks are perfectly aligned to the Cartesian coordinate lines. As a result, this system exhibits rather good convergence within standard FMM [10]. An analytical coordinate transformation is easily found by using a factorization of

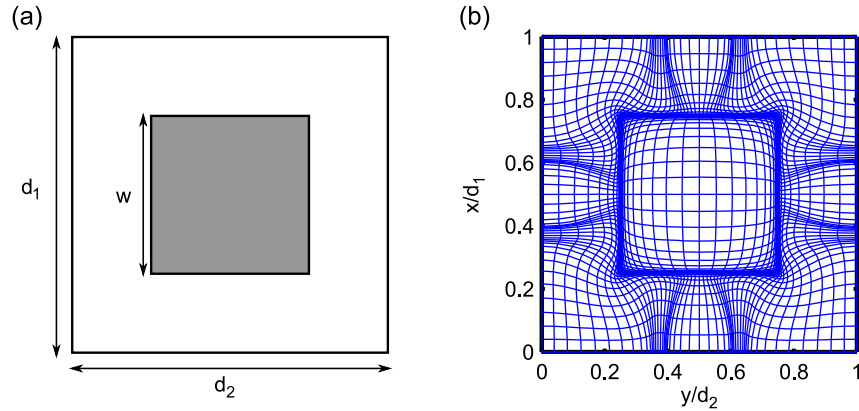


Fig. 3. (a) Schematic top view of the square-disk test structure and (b) automatically generated ASR via Eq. 14. See text for details.

the coordinate transformation into two one-dimensional transformations as described in Ref. [16]. In particular, we apply as one-dimensional transformation the same as used in Ref. [15] with parameter $G = 0.001$.

Our automatically generated ASR mesh for this structure is depicted in Fig. 3. This mesh has been generated with $M = 97$ plane wave coefficients, a smoothing width $w_s = 400$, and relative weights of the energy terms $\eta_c = 0.1$, $\eta_s = 0$, and $\eta_t = 0.1$. The \mathcal{C}_{4v} symmetry of the structure has been enforced in the minimization process. For further comparison, we have also generated a mesh with the tangential energy term switched off, i.e., with $\eta_c = 0.1$, $\eta_s = 0$, and $\eta_t = 0$ (not shown). This structure is normally illuminated by a plane wave with vacuum wavelength λ and linear polarization along the system's y -axis.

First, we check the convergence of the propagation constants (wave vectors in propagation direction) for a dielectric guest material with dielectric constant $\epsilon = 12$. The total resolution of the structure in real space is given on a 1024×1024 point grid. Table 1 shows our results on the convergence of the largest real-valued propagation constant q for standard FMM [10] and the three different ASR approaches (one analytical and two numerical transformations as described above) combined with FMM. More precisely, the analytical ASR and the numerical ASR with tangential energy term are identical up to the sixth significant digit, whereas the numerical ASR without tangential energy term exhibits a slightly worse convergence behavior. Even for this dielectric system, the calculation with standard FMM, i.e., without ASR, is not converged for the numbers N of plane waves that we have considered in this example.

Since we expect worse convergence characteristics for metallic structures, we have calculated the transmittance spectra of the same structure and have replaced the square dielectric disks by square metallic disks of the same dimension that are made from gold. In Fig. 4 (a), we display the corresponding transmittance spectra into the zeroth diffraction order for the four different approaches described above. All spectra have been calculated with $N = 317$ Fourier coefficients and, at first sight, rather good agreement between the different approaches is obtained. Nevertheless, we have examined the convergence characteristics of the system more carefully at the particle plasmon resonance of the square disk near $\lambda = 1600$ nm. In Fig. 4 (b), we display the convergence of the transmittance values into the zeroth diffraction order as a function of the number of plane waves N . The best convergence is reached for the analytical ASR, closely followed by the numerical ASR with tangential energy term. Based on this, we can draw the conclusion that grid-aligned structures can be treated rather satisfactorily within

Table 1. Convergence of first propagation constant $k_3 d_1$ (see Eq. (11) for a square array of square dielectric disks ($\epsilon = 12$) as a function of the number of plane waves (modes). The results for the largest purely real eigenvalue at $\lambda = 1600\text{nm}$ are shown. The eigenvalues, which are normalized to the lattice constant d_1 , have been calculated with standard FMM (Li), with analytical ASR (analytical), and numerically determined ASR via (i) minimization with tangential energy term (minT, Fig. 3 (b)) and (ii) without this (min). See the text for details about the system setup

Modes N	Li	analytical	minT	min
81	11.10136637	11.13011854	10.94312509	10.92452339
149	11.12409750	11.14779821	11.11683144	11.11483733
253	11.13158052	11.14818684	11.14632990	11.14585998
377	11.13469796	11.14817728	11.14808488	11.14784958
529	11.13621747	11.14817722	11.14813399	11.14797708
709	11.13704113	11.14817476	11.14813736	11.14800343
901	11.13752691	11.14817457	11.14814216	11.14803617
1129	11.13783207	11.14817429	11.14814738	11.14805258

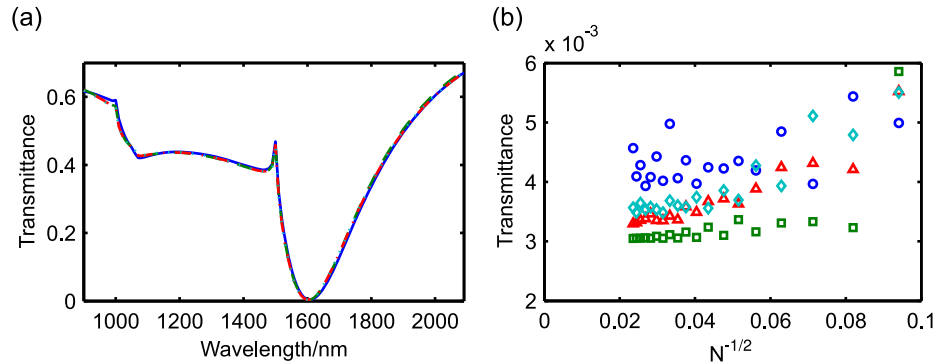


Fig. 4. Transmittance spectra (a) and convergence characteristics (b) for a square array of square gold disks. The computations have been carried out within standard FMM and three different ASR approaches within FMM: (a) Transmittance into the zeroth diffraction order within standard FMM (blue solid line), analytical ASR (green dashed line), numerical ASR with tangential term (red dash-dotted line), and numerical ASR without tangential term (dotted, cyan) using $N = 317$ plane waves; (b) Convergence characteristics for the transmittance into the zeroth diffraction order with $\epsilon = -122.03 + 12.85i$ (gold at $\lambda = 1600\text{nm}$) for standard FMM (blue open circles), analytical ASR (green open square), numerical ASR with tangential energy term (red open triangles), and numerical ASR without tangential term (cyan open diamonds).

standard FMM, i.e., without ASR. Even in this case, the use of ASR – be it analytical or numerical – within FMM provides a rather welcome convergence acceleration relative to standard FMM. Based on the inner workings of standard FMM (see section 1), we expect a significantly different behavior for the case of structures that are not grid aligned, so that in the next section, we turn to the analysis of such structures.

4.2. Circular disk

As second example, we consider a square array of circular metallic disks with height $h = 50$ nm and radius $r = 500$ nm (see Fig. 5 (a)). In order to generate the numerical ASR, we employ a reduced smoothing width $w_s = 200$ that accounts for the fact that the circular motif within the lateral plane does, in contrast to the square motif discussed in section 4.1, not exhibit any sharp corners. The corresponding parameters for the energy functional are kept the same, i.e., we use $\eta_c = 0.1$, $\eta_s = 0$, $\eta_t = 0.1$, employ $M = 97$ coefficients to describe the coordinate transformation, and enforce the \mathcal{C}_{4v} -symmetry of the structure. We depict the resulting ASR in Fig. 5 (b). This numerically generated ASR exhibits a certain degree of similarity with the analytical ASR that has been described in Ref. [17]. For convergence studies we have applied the approach of Ref. [17] in order to align the coordinate lines with the circular structure and map the circle onto a square. In a second step, we use the coordinate transformation described in Ref. [15] (with parameter $G = 0.01$) in order to increase the spatial resolution near material interfaces. The resulting meshes look similar to those shown in Ref. [17].

In Fig. 6, we depict the spectra for transmittance into the zeroth diffraction order of such a

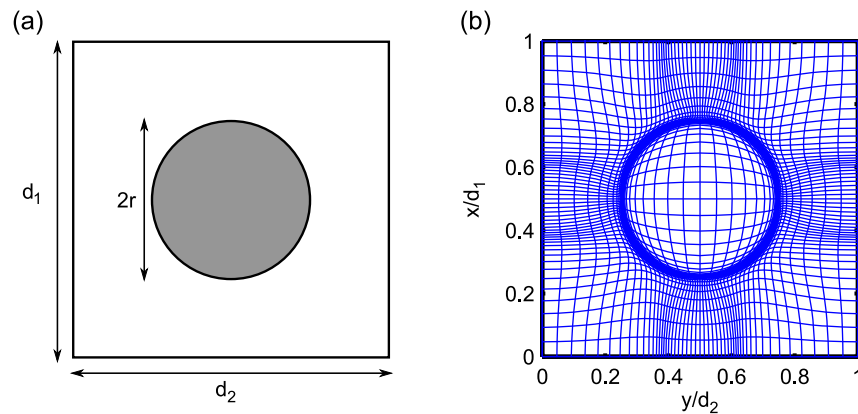


Fig. 5. (a) Schematic top view of the circular disk structure and (b) automatically generated ASR via Eq. 14. See text for details.

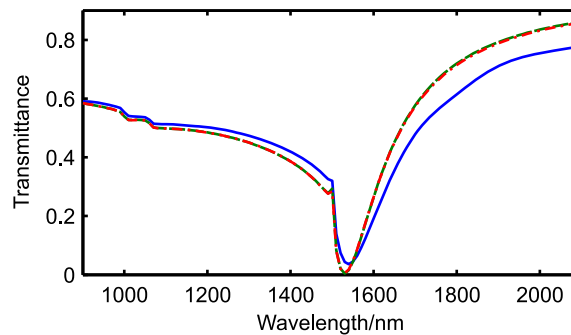


Fig. 6. Transmittance spectra into the zeroth diffraction order for a square array of circular disks. The computations have been carried out within standard FMM (blue solid line) with $N = 1257$ plane waves, analytical ASR within FMM (green dashed line) with $N = 317$ plane waves, and numerical ASR within FMM (red dash-dotted line) with $N = 317$ plane waves.

square array of circular metallic disks ($\epsilon = -110.9 + 11.24i$; corresponding to gold at $\lambda = 1530$ nm) that have been obtained within standard FMM ($N = 1257$ plane wave), analytical ASR within FMM ($N = 317$ plane waves), and numerical ASR within FMM with tangential energy term (see Fig. 5 (b); $N = 317$ plane waves). The spectra of both ASR approaches agree well and – as we will demonstrate below – are essentially converged to within 5 significant digits even for as few as $N = 317$ plane waves. In contrast, standard FMM is far from convergence even if as many as $N = 1257$ plane waves are employed.

In analogy to the square-disk case, we have examined the details of the convergence characteristics at the particle plasmon resonance, $\lambda = 1530$ nm. In Fig. 7 (a), we display the convergence behavior for the transmittance into the zeroth diffraction order as a function of the number N of plane waves. Clearly, both the analytical and the numerical ASR converge to the same value and $N = 317$ is sufficient to obtain convergence to within 5 significant digits. The results for standard FMM show a rather poor convergence. To further illustrate this, we have implemented the symmetry reduction technique for standard FMM described in Ref. [28] that – for given computational resources and normal incidence – allows us to push the number of plane waves significantly higher.

We display the corresponding results in Fig. 7 (b). Clearly, while the results for standard FMM start to approach the results for the ASR-based computations, there still are rather significant deviations even for the outrageously large number of $N = 23993$ plane waves.

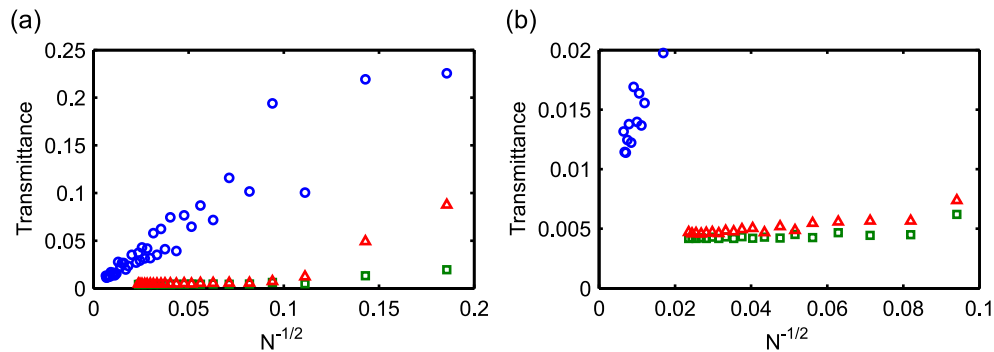


Fig. 7. Convergence characteristics of the transmittance into the zeroth transmittance order for a square array of circular metallic disks ($\epsilon = -110.9 + 11.24i$; gold at $\lambda = 1530$ nm). The computations have been carried out using standard FMM (blue open circles), analytical ASR (green open squares), and numerical ASR within FMM (red open triangles). The results depicted in panel (b) represent a close up of the results shown in panel (a). See text for details.

These results suggest that ASR, either in analytical or numerical form, is an absolute must for the accurate determination of the optical properties of non-grid-aligned metallic structures. In the subsequent section, we will, therefore, apply our numerical ASR technique to analyze a realistic system that consists of a square array of crescent-shaped metallic nano-particles. These and similar systems can be fabricated via shadow lithography and are thus of considerable interest [29–31]. To the best of our knowledge, analytic ASR results for these systems have not been published to date.

5. Realistic system

As a final illustration of our numerical ASR within FMM, we apply the approach to a square array of crescent-shaped optical antennas [29–31]. These structures lend themselves to a micro-fabrication approach based on colloidal templating and exhibit multiple plasmon resonances

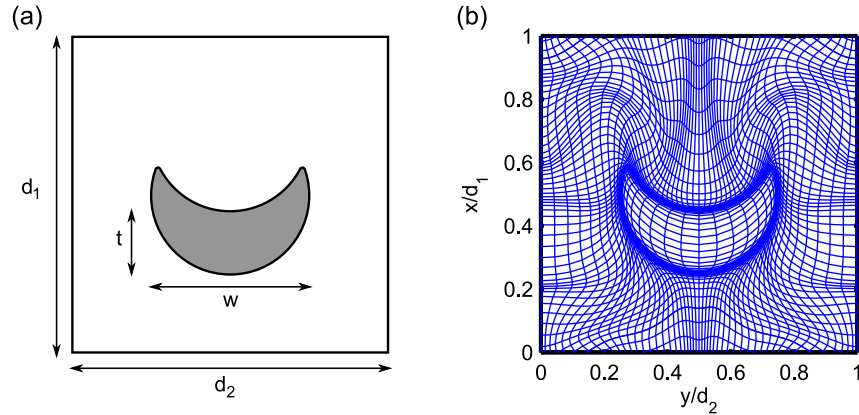


Fig. 8. (a) Schematic top view of the crescent-shape nano-antennas and (b) automatically generated ASR via Eq. 14. See text for details.

at visible and near infrared frequencies that may be exploited for applications ranging from surface enhanced Raman scattering (SERS) all the way to metamaterials. In Fig. 8 we provide a schematic of the lateral cross section and our numerical ASR for the specific value of the lateral width $w = 500$ nm and lateral thickness of $t = 200$ nm. In order to faithfully reproduce the actual experimental realizations we have added corner roundings, each with radius of 10nm, at the two tips. As for the previous structures, the height of the crescents is $h = 50$ nm and they are situated on a glass substrate.

For such situations with geometric features of different length scales and orientations, both the compression energy and tangential energy terms in Eq. 14 become more important. More precisely, the strong gradients near the tips tend to produce too high concentrations of points there relative to other areas of the crescent. This has to be counteracted by increasing the relative strength of the compression term. In addition, the large curvature near the almost semi-circularly shaped tips suggests that the coordinate lines should be very well adapted to the local

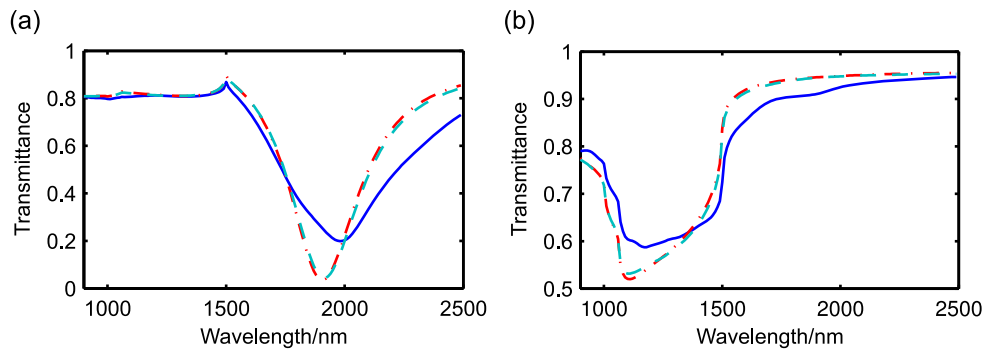


Fig. 9. Transmittance spectrum into the zeroth diffraction order for a square array of gold crescents that have been computed within standard FMM (blue solid line), numerical ASR with tangential term (red dash-dotted line) and numerical ASR without tangential term (cyan dashed line). The calculations have been carried out for y -polarized excitation (curves with pronounced resonances near $\lambda \approx 1900$ nm) as well as for x -polarized excitations (curves with pronounced resonances near $\lambda \approx 1100$ nm).

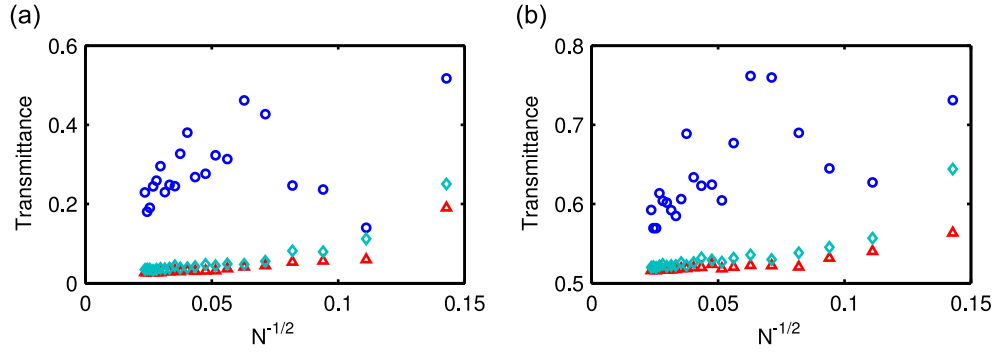


Fig. 10. Convergence characteristics of the transmittance into the zeroth transmittance order for a square array of metallic crescents made from gold. The computations have been carried out using standard FMM (blue open circles), numerical ASR with tangential energy term (red open triangles), and numerical ASR without tangential term (cyan open diamond) within FMM. Panel (a) depicts the case of y -polarized excitation at $\lambda = 1900$ nm with $\epsilon = -175.08 + 21.43i$ (gold at $\lambda = 1900$ nm) and panel (b) depicts the case of x -polarized excitation at $\lambda = 1100$ nm with $\epsilon = -53.21 + 4.20i$ (gold at $\lambda = 1100$ nm).

geometry, thus calling for an increased relative weight of the tangential energy term. Consequently, we have generated the ASR depicted in Fig. 8 (b) with the same smoothing width $w_s = 200$ and the same number $M = 97$ of Fourier coefficients as before but have used different relative weights of the energy terms according to $\eta_c = 0.2$, $\eta_s = 0$, and $\eta_t = 0.2$ and enforce the mirror symmetry of the structure. Here, we choose different weights as in section 4 since the crescent shape has smaller features and thus the weights have to be larger as otherwise the gradient contribution would become too large at these points. In turn, this would lead to an absurdly large point density at that same grid position.

Since we have no analytical meshes for comparing our results, we generate a second numerical mesh for comparison, this time without tangential energy term using the parameters $w_s = 200$, $\eta_c = 0.2$, $\eta_s = 0$, and $\eta_t = 0$ (not shown).

In Fig. 9, we depict the transmittance spectra into the zeroth diffraction order for x - and y -polarized illumination by normally incident plane waves. Similar to the case of the circular disk array, standard FMM with $N = 1257$ reciprocal lattice vectors is not converged while the computations that utilize numerical ASR within FMM require only $N = 317$ reciprocal lattice vectors to achieve well converged results (see also Fig. 10). A comparison of these spectra with the corresponding spectra of U-shape nano-particles (see Ref. [1]) reveals that there exists a close similarity between the two systems. Specifically, for the crescent array the so-called electric resonance under x -polarized excitation is located at $\lambda = 1100$ nm (see also Fig. 11 (b)) while the so-called magnetic resonance under y -polarized excitation is located at $\lambda = 1900$ nm (see also Fig. 11 (a)). These resonances as well as Rayleigh anomalies due to the periodicity of the array are clearly observed in the numerical ASR within FMM results.

As before, we carefully check the convergence of the different methods for wavelengths near these resonances and display the corresponding results in Fig. 10. Loosely speaking, we obtain essentially the same convergence characteristics of standard FMM and numerical ASR within FMM as in the case of the circular disk array.

One of the major advantages of ASR is the increased resolution near the two tips of the crescent. This becomes particularly useful when the field distributions in the structure have to be determined, for instance, in order to assess the structure's usefulness regarding applications as a

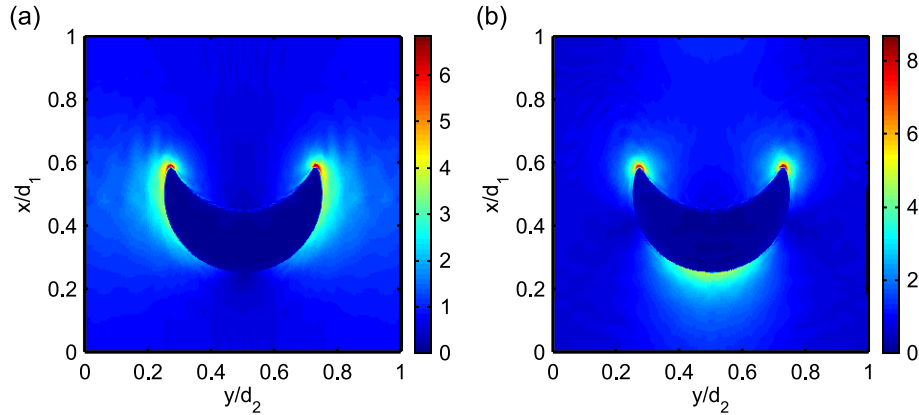


Fig. 11. Magnitude of the electric field enhancement for a square array of gold crescent-shaped nano-particles. Panel (a) depicts the field enhancement at the magnetic resonance at $\lambda = 1900\text{nm}$ (y -polarized excitation) and panel (b) depicts the field enhancement at the electric resonance at $\lambda = 1100\text{nm}$ (x -polarized excitation).

SERS substrate or other nonlinear optical phenomena. The electromagnetic fields can be directly computed in the curvilinear coordinate system provided by ASR so that the resulting high spatial resolution near material interfaces in the Cartesian coordinate frame directly translates into well-resolved fields. We have calculated the electric fields at the so-called magnetic and electric resonances using the numerical ASR within FMM with $N = 1257$ reciprocal lattice vectors. A comparison with results for different numbers of plane waves yields that these field values are within 5% of the converged results. The corresponding enhancement of the electric field in a plane 25 nm above the glass substrate, i.e., halfway through the metal film that is 50 nm high, are shown in Fig. 11 (a) and (b), respectively. The field enhancement at the tips is clearly visible and the field distributions of these modes are rather similar those of their counterparts at the electric and magnetic resonances of U-shaped nanoparticles [1].

6. Conclusion

In summary, we have applied Li's anisotropic formulation of the standard FMM to Maxwell's equations in curvilinear coordinates for the realization of ASR. For a given periodic structure, i.e., lattice type and shape of the object within the unit cell), the curvilinear coordinates are *automatically generated* through the minimization of an appropriate fictitious energy functional in such a way that (i) the point density near material interfaces is increased and (ii) one of the coordinate lines is (locally) aligned parallel relative to the material boundary that is provided by the local shape of the object. While an energy functional that incorporates the former aspect has been used in the context of bandstructure computations before [20], our additional tangential energy term incorporates the latter aspect and this becomes particularly important for complex geometric features such as the array of metallic crescents which we have considered in this work.

For simple test structures where analytical meshes are available, we have compared our numerical ASR approach with corresponding computations for analytical ASR and have found very good agreement. In essence, standard FMM (without ASR) works reasonably well for grid-aligned dielectric and metallic structures but even in these cases ASR provides considerable convergence acceleration. For non-grid-aligned structures, standard FMM can still be used for dielectric systems (albeit with significantly increased computational effort), but for metallic

structures ASR either in analytical or numerical form becomes an absolute must.

In order to demonstrate the versatility of our approach, we have computed the optical properties of a rather complex structure, i.e., a square array of gold crescents [29, 30], for which no analytical ASR exists to date and which exhibits complex geometric features on different scales without grid alignment. Our numerical ASR approach within FMM provides highly accurate results for transmittance spectra and field enhancements with rather modest computational resources. Our automatized mesh generation can be applied to arbitrarily shaped objects and, therefore, our approach results in a flexible and efficient tool for the investigation of arrays of metallic nanoparticles using numerical ASR within FMM.

Acknowledgement

We acknowledge support by the Deutsche Forschungsgemeinschaft (DFG) and the State of Baden-Württemberg through the DFG-Center for Functional Nanostructures (CFN) within sub-projects A1.1, A5.2, and A5.6. The research of S.E. is embedded in the Karlsruhe School of Optics & Photonics (KSOP). Some computations have been performed on HP XC4000 at Steinbuch Center for Computing (SCC) Karlsruhe under project NOTAMAX. It is a pleasure to thank Thomas Zebrowski for numerous discussions and critical reading of the manuscript.